

Review Article

Recent Advances in Ferroelectric Nanosensors: Toward Sensitive Detection of Gas, Mechano-thermal Signals, and Radiation

Krystian Mistewicz 

Institute of Physics – Center for Science and Education, Silesian University of Technology, Krasińskiego 8, 40-019 Katowice, Poland

Correspondence should be addressed to Krystian Mistewicz; krystian.mistewicz@polsl.pl

Received 15 June 2018; Revised 17 August 2018; Accepted 23 August 2018; Published 25 November 2018

Academic Editor: Victor M. Castaño

Copyright © 2018 Krystian Mistewicz. This is an open access article distributed under the Creative Commons Attribution License, which permits unrestricted use, distribution, and reproduction in any medium, provided the original work is properly cited.

A spontaneous polarization that occurs below the Curie temperature is characteristic for ferroelectric materials. This polarization is sensitive to many external conditions such as an electric field, mechanical deformation, temperature, and chemical and biological factors. Therefore, bulk ferroelectric materials have been used for decades in sensors and actuators. Recently, special attention has been paid to ferroelectric nanostructures that represent better sensing properties than their bulk counterparts. This paper presents a comprehensive survey of applications of nanoferroelectrics in different types of sensors, e.g., gas sensors and piezoelectric, pyroelectric, and piezoresistive sensors of mechano-thermal signals, as well as photodetectors, ionizing radiation detectors, and biosensors. The recent achievements and challenges in these fields are summarized. This review also outlines the prospects for future development of sensors based on nanosized ferroelectrics.

1. Introduction

Ferroelectricity was observed for the first time in Rochelle salt nearly a century ago [1]. This property of crystal is recognized as an occurrence of a spontaneous polarization. It originates from an asymmetric crystal structure which can induce nonoverlapping charges in unit cell centers leading to formation of a steady electric dipole moment. A spontaneous polarization of a ferroelectric can be switched between different stable orientations by use of an electric field of sufficient magnitude, known as the coercive field.

In the last decade, nanoscale ferroelectrics [2–4] have been investigated with increasing intensity. They exhibit numerous excellent properties such as direct and inverse piezoelectricity, pyroelectricity, ferroelectric photovoltaicity, and nonlinear optical activity. This exceptional combination of various properties makes them attractive for application in field effect transistors [5], nonvolatile memories [6], capacitors [7, 8], photovoltaic cells [9, 10], actuators [11], piezoelectric energy harvesters [8, 12–15], thermal imaging cameras, and electro-optic devices [16]. Nanoferroelectrics are also commonly used in sensors, since the polarization is influenced by various external conditions, including an electric

field, mechanical deformation, temperature, and chemical and biological factors.

Zero- and one-dimensional ferroelectric nanomaterials have been fabricated using different processing methods, e.g., vapor-phase (Sb_2S_3 nanowires [17], SbSI nanorods [18]), hydrothermal (BaTiO_3 nanowires [14, 19–21], BaTiO_3 nanoparticles [22], BiFeO_3 [23], KNbO_3 nanorods [24], KNbO_3 nanowires [25]), solvothermal (LiNbO_3 nanocrystals [26]), colloidal (Sb_2S_3 nanowires [27]), sol-gel (PbTiO_3 nanotubes [28, 29]), mechanochemically assisted ($\text{Bi}_4\text{Ti}_3\text{O}_{12}$ [30]), electrospinning (BiFeO_3 nanofibers [9], poly(vinylidene fluoride) nanofibers [31]), and sonochemical (SbSI nanowires [32–35]). More information about recent trends in fabrication techniques of 0D and 1D ferroelectric nanomaterials can be found elsewhere [2, 36].

Ferroelectric thin films show great potential for use in flexible sensing devices [37, 38], e.g., electronic skin (e-skin). Essential papers on development of new materials for e-skin have been published by Bao's research group [39, 40]. A significant effort in the integration of ferroelectric films with flexible electronics has been made by Calzada and coworkers [41–44]. For example, they developed a photocatalytically assisted decomposition of liquid precursors of metal oxides

incorporating TiO_2 particles [43] for the preparation of ferroelectric $\text{Pb}(\text{Zr}_{0.3}\text{Ti}_{0.7})\text{O}_3$ and multiferroic BiFeO_3 perovskite thin films. In another work [44], they presented low-temperature fabrication of BiFeO_3 thin films directly on flexible polyimide substrates.

The finite size effects, observed for low-dimensional materials, are responsible for new physical phenomena. Comparing nanosized ferroelectrics to bulk crystals, one can notice modifications of physical properties, i.e., differences in values of Curie temperatures, dielectric constants, coercive fields, and piezoelectric response levels [2]. It is worth mentioning that the ferroelectric nanostructures are supposed to represent higher sensitivity in respect to their bulk counterparts [45].

This paper is focused on application of ferroelectric nanomaterials in sensing devices and presents latest achievements in this quickly developing field. Different types of sensors are reviewed: gas sensors and piezoelectric, pyroelectric, and piezoresistive sensors of mechanothermal signals, as well as photodetectors, ionizing radiation detectors, and biosensors.

2. Gas Sensors

2.1. Adsorbate Interactions with Ferroelectric Surface. During the last decade, huge effort has been made to understand mechanisms of gas adsorption on ferroelectrics [46–53]. The polarization of a ferroelectric domain (c^+/c^-) has been found to have a significant effect on the surface properties. In 2008, Li et al. studied the interaction of carbon dioxide with BaTiO_3 and $\text{Pb}(\text{Ti}_{0.52}\text{Zr}_{0.48})\text{O}_3$ surfaces [46]. They discovered that the impinging gas molecules can become trapped into a shallow physisorption, dominated by van der Waals interactions and influenced by polarization [46, 51]. The trapped molecules may move along the surface. Many of them spend a short time on the surface and then desorb. The chemisorbed species is formed, when the molecule, with sufficient energy to overcome an activation barrier, encounters an active site (e.g., an oxygen vacancy) [46]. A molecular adsorption of CO_2 at defect sites is the most energetically favorable mode of adsorption on the negatively poled surface (c^-) due to the fact that oxygen vacancies compensate the polarization charge and dissociative adsorption of CO_2 . It results in filling of the vacancy being less energetically favorable.

It was well documented that the dipole moment of a polar molecule may interact with the electric polarization of some domains on the ferroelectric surface [46, 47, 49, 52–54]. Consequently, the strength of molecular adsorption is increased [49, 51]. A comparison of polar and nonpolar molecule adsorption on oppositely poled LiNbO_3 surfaces was provided by Yun et al. in [54]. They proved stronger adsorption of 2-propanol on the positively poled surface and concluded that interactions between polar molecules and the ferroelectric surface are dominated by electrostatics [54]. The scanning tunneling microscopy investigations of the BaTiO_3 (001) surface [47] revealed the strong chemisorption of carbon dioxide on the c^+ ferroelectric domain and a weak interaction between CO_2 and the c^- domain. Usually, this

polarization-dependent adsorption is attributed to a dipole-dipole interaction between the gas molecule and ferroelectric surface or it is explained by taking into account the differences in surface chemistry influenced by polarization variations [53].

2.2. Ferroelectric Nanomaterials for High-Sensitivity Gas Detection. The high surface-to-volume ratio of ferroelectric antimony sulfide (SbSI) nanowires makes them especially attractive for gas sensing applications. Starczewska et al. [32] for the first time presented the effect of water vapor on the electrical response of SbSI xerogel to explore its application as a humidity sensor. SbSI was prepared sonochemically from the constituents (the elements antimony, sulfur, and iodine). The used experimental setup and applied procedure were the same as described in [33]. SbSI xerogel (Figures 1(a) and 1(b)) was composed of nanowires with average lateral dimensions of 10–50 nm and lengths up to several micrometers. The impedance spectroscopy studies revealed that electric resistance decreased by three orders of magnitude with the increase in relative humidity (RH) from 10% to 85%. This high sensitivity of SbSI nanowires to humidity changes was explained taking into account dissociation of water molecules on the SbSI surface and generation of mobile protons. As it was proposed elsewhere [33–35], the humidity sensing mechanism relies on Grotthuss' chain reaction [55], where proton transfer occurs in hydronium and an ion-conductive layer is formed on the surface of SbSI nanowires.

Recently, a simple route [56] for preparation of functional devices containing a few SbSI nanowires (Figures 1(c) and 1(d)) has been established. It has involved dispersion of SbSI xerogel in toluene, deposition of dispersed solution on special substrate equipped with microelectrodes, electric field-assisted alignment of nanowires, and their bonding to microelectrodes using ultrasonic nanowelding. Such prepared devices have been successfully applied for humidity sensing [35, 57], as well as for detection of different gas molecules (H_2 [58], O_2 [58], and N_2O [56], CO_2 [35]). Comparing properties of humidity sensors made of an array of a few aligned SbSI nanowires and SbSI xerogel, it was concluded in [35] that latter one exhibits longer time response and simultaneously higher sensitivity to humidity changes. It was probably due to water adsorption in the form of clusters of H_2O molecules agglomerated on the nanowire boundaries and near the contacts between nanowires. An electric current response of SbSI nanowires to humidity changes was found to be exponential [33, 35]. A similar behavior was observed for ferroelectric potassium niobate (KNbO_3) nanofibers by Ganeshkumar et al. [59]. In this work, high-quality ferroelectric KNbO_3 nanofibers were synthesized via the electrospinning method. Then, a fabricated nanomaterial was used for fast and accurate humidity sensing, displaying a logarithmic-linear dependence behavior of an electric conductance with relative humidity. Similar to [35], mobile protons were found to be responsible for a strong increase in electrical conductivity due to water physisorption on the grain boundaries and flat surfaces of potassium niobate [59]. Nanosensors based on KNbO_3 nanofibers exhibited

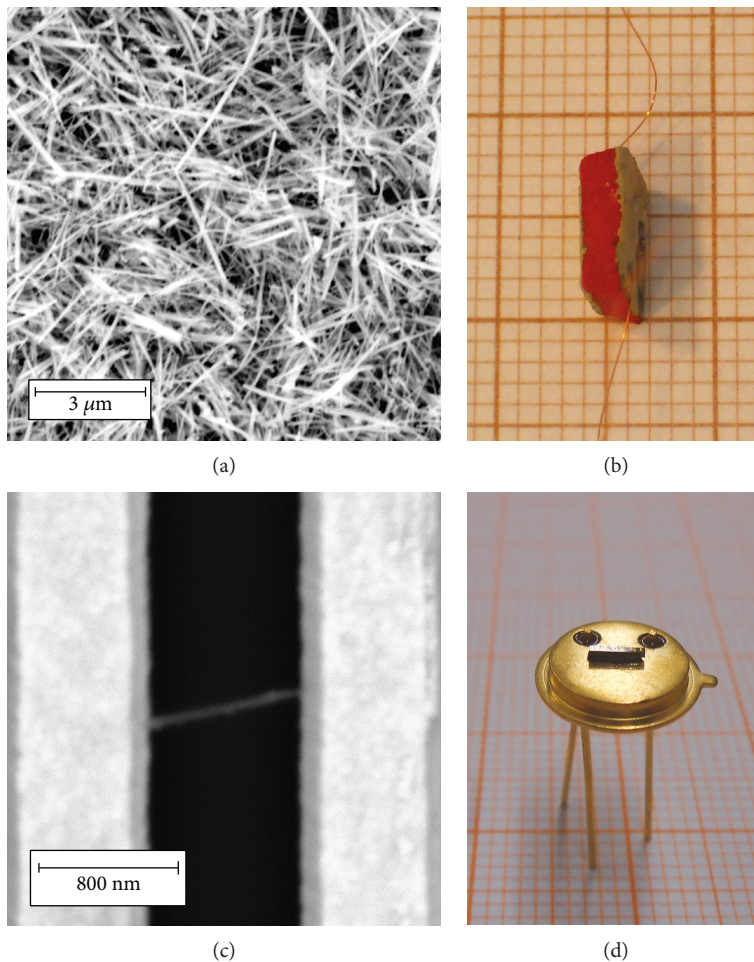


FIGURE 1: (a) Scanning electron micrograph of a part of sensor (b) constructed from sonochemically prepared SbSI xerogel; (c) SEM micrograph of a single nanowire (a part of an array of a few nanowires) aligned in the electric field and bonded ultrasonically to Au microelectrodes on Si/SiO₂ substrate that was integrated in standardized metal semiconductor package TO-5 (d). Reprinted from [35] under the terms of the Creative Commons Attribution 4.0 International License.

excellent sensing performance: a sensitivity of four orders in magnitude with respect to RH changes from 15% to 95%, short response (2 s), and recovery (10 s) times as well as good reproducibility.

The investigations of electric responses of the SbSI nanosensor to donor (Figures 2(a) and 2(b)) and acceptor (Figures 2(c) and 2(d)) gases allowed determining an electrical conductivity type of SbSI nanowires [58]. An adsorption of oxygen and hydrogen resulted in an increase and decrease in electric current flowing through the SbSI nanosensor, respectively [58]. Such behavior indicated the p-type conductivity of SbSI nanowires. The reversible character of the response of the SbSI nanosensor to oxygen and hydrogen, realized by simple evacuation of gas from the test chamber, suggested that H₂ and O₂ molecules are physisorbed on the SbSI surface. The physisorption was dominated by van der Waals interactions and influenced by ferroelectric polarization [58]. The temperature dependences of electric current $I(T)$ flowing through semiconducting SbSI nanowires in vacuum, as well as in oxygen and hydrogen atmosphere, were also measured (Figure 2(e)). They exhibited a typical ferroelectric behavior; i.e., the slopes of characteristics $I(T)$

changed near Curie temperature (T_C). The $I(T)$ dependences were least squares fitted in the paraelectric and ferroelectric regions using the following relation:

$$I(T) = I_0 \cdot \exp\left(-\frac{E_A}{k_B T}\right), \quad (1)$$

where E_A is the activation energy, I_0 represents the proportionality factor, and k_B and T have their usual meanings. Table 1 presents the values of the fitted parameters and phase transition temperatures. The latter ones were evaluated as intersections of straight-line extrapolations below and above the knee of $I(T)$ characteristics (Figure 2(e)). Values of T_C determined for SbSI nanowires in O₂ and H₂ (Table 1) were a little higher than T_C in vacuum. It was recognized as well known the influence of adsorbates on phase transitions in ferroelectrics [60].

Thin films of other ferroelectric materials (i.e., (Ba, Sr)TiO₃ [61–63] and Pb(Zr, Ti)O₃ [63, 64]) were applied by Zhu and coworkers for detection of hydrogen gas. In the case of all of these capacitor-type hydrogen sensors, the presence

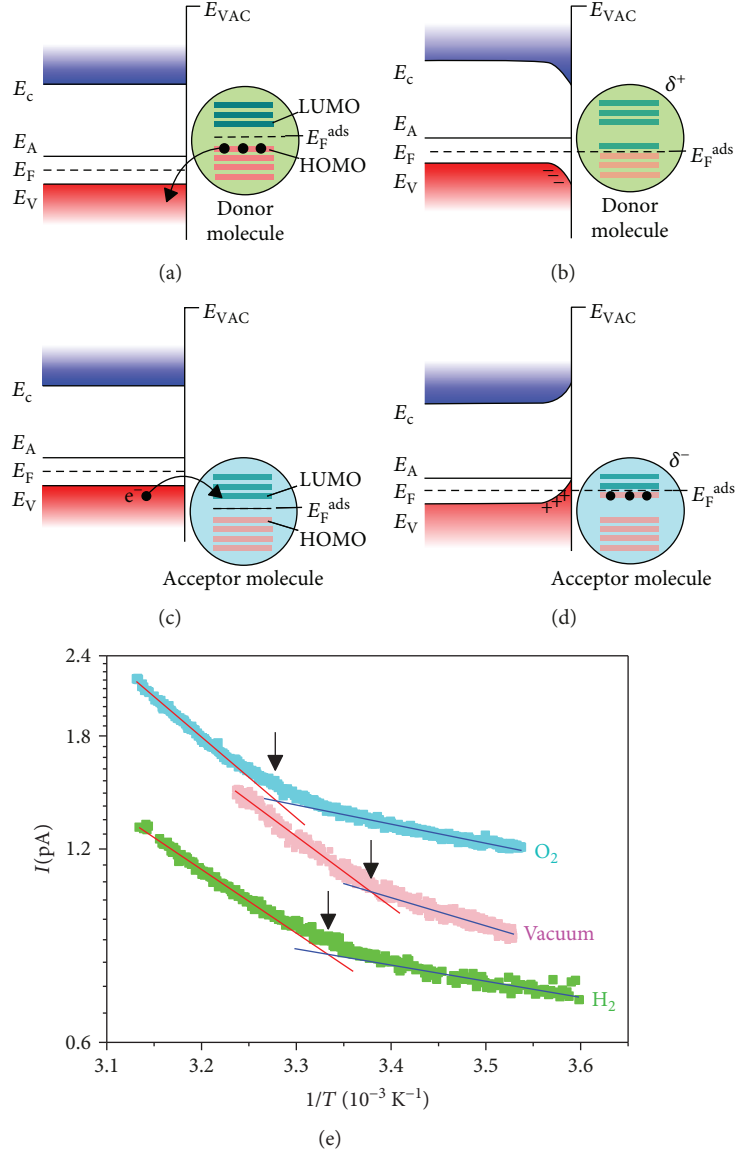


FIGURE 2: Band model of a p-type semiconductor before (a, c) and after adsorption of the donor (b) and acceptor (d) gas molecule; E_V , E_C : bottom and top of energy gap; E_A : acceptor level; E_F , E_F^{ads} : Fermi levels of semiconductor and adsorbate; LUMO, HOMO: lowest unoccupied and highest occupied molecular orbitals; E_{VAC} : electron energy in vacuum; (e) temperature dependence of electric current flowing through SbSI nanowires in O_2 $p = 4 \cdot 10^4$ Pa (blue-green square), H_2 $p = 4 \cdot 10^4$ Pa (green square), and vacuum $p = 10^{-1}$ Pa (pink square) (RH = 0%, $E = 1.5 \cdot 10^6$ V/m). Blue and red lines represent the fitted (1) in ferroelectric and paraelectric phases, respectively. The arrows show Curie temperatures. Values of fitted parameters are given in Table 1. Reprinted from [58]. Copyright (2016), with permission from Elsevier.

of H_2 molecules in air led to a decrease in Schottky barrier height through charges induced by hydrogen ions at the metal/ferroelectric interface. It was measured as a shift of current-voltage characteristics of the devices under a hydrogen-containing atmosphere. Zhu et al. concluded that the high permittivity of the amorphous ferroelectric thin films enhanced the proton polarization at the metal/ferroelectric interface and, in turn, greatly improved the built-up interfacial potential induced by hydrogen [62].

The array of a few SbSI nanowires was also applied to sensitive detection of carbon dioxide gas in dry nitrogen

[35]. The response of the SbSI nanosensor to different concentrations of CO_2 (Figure 3(a)) was fitted with the following empirical dependence

$$\Delta I_{\text{CO}_2} = \Delta I_0 \cdot c^\varphi, \quad (2)$$

where ΔI_{CO_2} denotes the change in sensor current at a certain CO_2 concentration (c), $\Delta I_0 = 9.3(12)$ fA represents the pre-exponential factor, and the power coefficient $\varphi = 0.162(15)$ is related to the responsivity of an electrical conductivity of SbSI nanowires on changes of analyte gas amount. An influence of CO_2 concentration on sensitivity of the SbSI

TABLE 1: Parameters of (1) fitted to temperature dependence of electric current flowing through SbSI nanowires (Figure 2(e)) in different gas atmospheres. Reprinted from [58]. Copyright (2016), with permission from Elsevier.

Gas atmosphere	Pressure p (Pa)	E_A (eV)		T_C (K)
		In ferroelectric phase	In paraelectric phase	
Vacuum	10^{-1}	0.087 (3)	0.218 (4)	295.9 (2)
Hydrogen	$4 \cdot 10^4$	0.050 (3)	0.197 (3)	300.0 (2)
Oxygen	$4 \cdot 10^4$	0.059 (1)	0.249 (2)	305.0 (2)

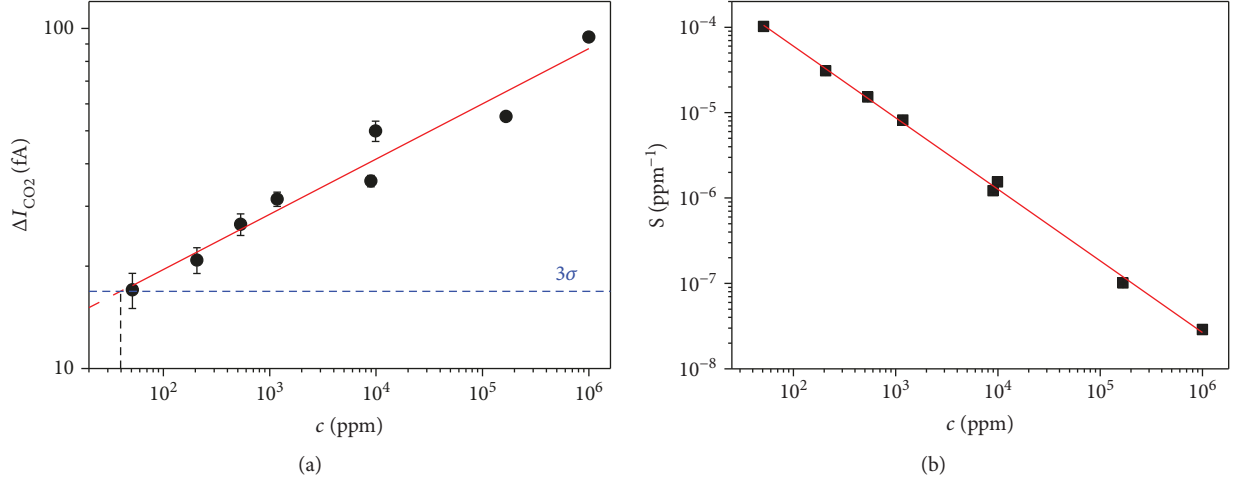


FIGURE 3: Current response (a) and sensitivity (b) of an array of a few SbSI nanowires as a function of CO_2 concentration ($T = 304$ K, $E = 1.5 \cdot 10^6$ V/m, $p = 9.8 \cdot 10^4$ Pa); red solid lines represent the best fitted dependences described by (2) and (3); values of the fitted parameters are presented in the text; blue dashed line represents three times the standard deviation of the noise. Reprinted from [35] under the terms of the Creative Commons Attribution 4.0 International License.

nanosensor (Figure 3(b)) was fitted using the following relation [35].

$$S = S_0 \cdot c^{\varphi-1}, \quad (3)$$

where $S_0 = \Delta I_{\text{CO}_2}/I_0$ and I_0 is the reference value of the sensor exposed to dry nitrogen (without the CO_2). The sensitivity was found to decrease the sensitivity with increasing gas concentration (Figure 3(b)). It suggested that with the rise in the number of adsorbed CO_2 molecules, the density of active sites on the SbSI surface is reduced. The increase in electric conductance of SbSI nanowires upon exposure to CO_2 was attributed to formation of $\text{CO}_2^{\delta-}$ species interacting with the p-type SbSI surface [35]. The sensor based on SbSI nanowires was able to detect as low CO_2 concentration as 40(31) ppm.

The most recent application of a few aligned SbSI nanowires was their use in ammonia gas sensors [65]. The comparable values of detection limits 6.0(24) ppm and 6.3(39) ppm were determined at operating temperatures of 280 K and 304 K, respectively. It should be underlined that these values are noticeably less than the recommended threshold limit value for human exposure to ammonia (50 ppm [66]) and they are competitive to parameters of other conductometric NH_3 nanosensors [65]. A significantly higher response and sensitivity of the sensor were observed, when the operating temperature was lower than Curie temperature. It was suggested that strong interaction between ferroelectric domains

and electric dipole moments of ammonia molecules was responsible for huge sensor response reaching over 800% at an operating temperature of 280 K [65]. The SbSI nanosensor demonstrated a high selectivity to NH_3 against other interfering gases (H_2O , CO_2 , O_2 , H_2 , N_2O , and CO). Moreover, it exhibited good stability and short-term response reversibility and did not require a heating system for recovery.

Wang et al. [49] proposed a ferroelectric nanosensor for noninvasive monitoring of acetone in exhaled breath. It was constructed using a mixture of tungsten trioxide polymorph ($\epsilon\text{-WO}_3$) and Cr-doped WO_3 nanoparticles. This material has an acentric structure, where the polarity is affected by the displacement of tungsten atoms from the center of each $[\text{WO}_6]$ octahedral [49]. The lowest concentration of acetone, detected by the WO_3 -based nanosensor, was 0.2 ppm. The sensor response was also tested for other gases (e.g., ethanol, methanol, NH_3 , NO_2 , NO , and CO). It was found that the interaction between the $\epsilon\text{-WO}_3$ surface dipoles and large electric dipole moments of acetone molecules led to high selectivity to this gas detection [49].

In 2016, Chakradhar Sridhar et al. [67] developed a polymerization method for fabrication of polyaniline (PANI) and indium oxide (In_2O_3) nanocomposites. These materials exhibited applicability for detection of liquefied petroleum gas (LPG). An electric resistance of PANI/ In_2O_3 nanocomposites enhanced with LPG concentration increase. Maximum sensitivity for gas sensing was observed for composite of 50 wt% In_2O_3 in polyaniline [67].

3. Sensors of Static and Dynamic Mechano-thermal Signals

3.1. Pyroelectric Sensing. Pyroelectricity refers to electric charge generation mechanisms along specific crystallographic directions driven by changes in crystal temperature [2]. In [68], it was proved that the pyroelectric coefficient of ferroelectric nanowires strongly increases with the decrease in nanowire radius. This size-driven enhancement of pyroelectric coupling can lead to the giant pyroelectric current and voltage generation by the polarized ferroelectric nanoparticles in response to the temperature fluctuation [68].

Zirkl et al. proposed a low-cost fabrication route [69] for a new generation of large-area flexible control and input interfaces based on ferroelectric active matrix sensor networks and printed displays. The matrix sensor array was printed using only five functional inks: fluoropolymer P(VDF-TrFE) (poly(vinylidene fluoride trifluoroethylene)), the conductive polymer PEDOT:PSS (poly(3,4-ethylenedioxythiophene):poly(styrene sulfonic acid)), a conductive carbon paste, a polymeric electrolyte, and a photoresist separation layer. Each pixel of the sensor array consisted of a 5 μm thick film of P(VDF-TrFE) and electrochemical transistor (ECT) acting as sensing layer and the read-out unit, respectively. For touchless control of the active matrix sensor, the pyroelectric operation mode was employed, whereas touch-based control was enabled by piezoelectricity of P(VDF-TrFE). A temperature or pressure change generated electric charges in the thin film of the ferroelectric polymer, which affected an electric current of the ECT and induced complete on/off switching. Finally, the responses of the pixels were visualized by means of a flexible electrochromic display connected to the output of the sensor array.

Recently [70], Park et al. have developed a multimodal e-skin using a ferroelectric polymer composite (Figure 4(a)) that contained poly(vinylidene fluoride) (PVDF) and reduced graphene oxide (rGO). This novel e-skin was able to detect simultaneously static and dynamic pressure, temperature changes, and vibrations. Moreover, it discriminated between these stimuli via different signal generation modes such as sustained pressure (piezoresistive), temporal pressure (piezoelectric), and temperature (pyroelectric). The negative temperature coefficient (NTC), observed for an rGO/PVDF composite film (Figures 4(b) and 4(c)), was explained due to the change in the contact resistance between the rGO sheets by thermomechanical variation as well as the intrinsic NTC behavior of rGO [70]. Park et al. demonstrated that the rGO/PVDF composite film can be successfully applied as flexible temperature-sensitive e-skin (Figure 4(d)). It was achieved by placing an array of 216 gold electrodes on the top and bottom of the film. Such prepared device was used for temperature mapping of a human hand placed on the e-skin, as shown in Figure 4(d). Moreover, an electric resistance of the e-skin was further investigated immediately after contact with a water droplet at various temperatures monitored by an infrared (IR) camera (Figure 4(e)). The dashed and solid lines, depicted in Figures 4(f) and 4(h), represent time dependence of droplet temperature and e-skin resistance, respectively. The initial variation of the

e-skin resistance (for $t < 0.2$ s) was described using the following equation [70].

$$\frac{R}{R_0}(t) = \left(\frac{R}{R_0}\right)_{\text{L.E.}} + \left[1 - \left(\frac{R}{R_0}\right)_{\text{L.E.}}\right] \exp\left(-\frac{t}{\tau_T}\right), \quad (4)$$

where R denotes e-skin resistance and τ_T is the characteristic time of resistance changes.

The best fitting of the experimental data to (4) was obtained for $\tau_T = 11$ ms, confirming usability of the e-skin, based on the rGO/PVDF composite film, for fast monitoring of temporal and spatial variation of temperature.

3.2. Piezoelectric Sensing. Piezoelectricity is related to the generation of opposite electric charges on the surfaces of a crystal, when it is subjected to directional stress or under hydrostatic stresses [2]. In the current section, the most important achievements in an emerging field of nanosized piezoelectric sensors are highlighted.

Over the past 20 years, the integration of ferroelectric thin films into microelectromechanical systems (MEMS) [71–73] has revolutionized the research in piezoelectric microsensors. The large piezoelectric response available in ferroelectric films enables low-voltage operation of high-sensitivity sensors [72]. The lead zirconate titanate (PZT) represents a family of ferroelectric materials which have been the most widely utilized in MEMS sensors. One should remember that the values of piezoelectric coefficients of PZT films are influenced by many factors, like film orientation, composition, grain size, defect chemistry, and mechanical boundary conditions. Numerous papers [71–75] have been published on strain measurements realized using cantilever-like MEMS sensors based on PZT thin films. A deformation of this flexible structure can be monitored by measurement of piezoelectric charges generated due to in-plane strain. Furthermore, thin films of PZT have been also frequently applied in piezoelectric micromachined ultrasound transducers (PMUTs) [76].

Graz and coworkers presented that a ferroelectret film can be mechanically and electrically interfaced with the amorphous silicon field-effect transistor via a thin dielectric coupling layer [77]. The ferroelectrets [78] exhibit ferroelectric-like hysteresis, switching, and a pronounced longitudinal piezoelectric effect with high piezoelectric coefficients [77]. Graz et al. laminated a cellular polypropylene film and amorphous Si thin-film transistor on polyimide substrate. Such prepared device demonstrated the ability to respond in a static capacitive or dynamic piezoelectric mode. The flexible ferroelectret field-effect transistor was applied as a pressure-activated switch, a microphone, and a touch sensor suitable for integration in e-skin.

A novel ultrasensitive strain sensor, based on PVDF thin film, has been recently developed by Lu et al. [79]. The proposed sensor array consisted of 16 microcapacitor units with a 4×4 square structure, which were patterned on polydimethylsiloxane (PDMS) substrate. The voltage signals of 20–300 mV were generated, when a pressure in the range of 60–150 kPa was applied to the sensor [79]. The device exhibited ultra-high sensitivity of 12 mV/kPa and extremely fast

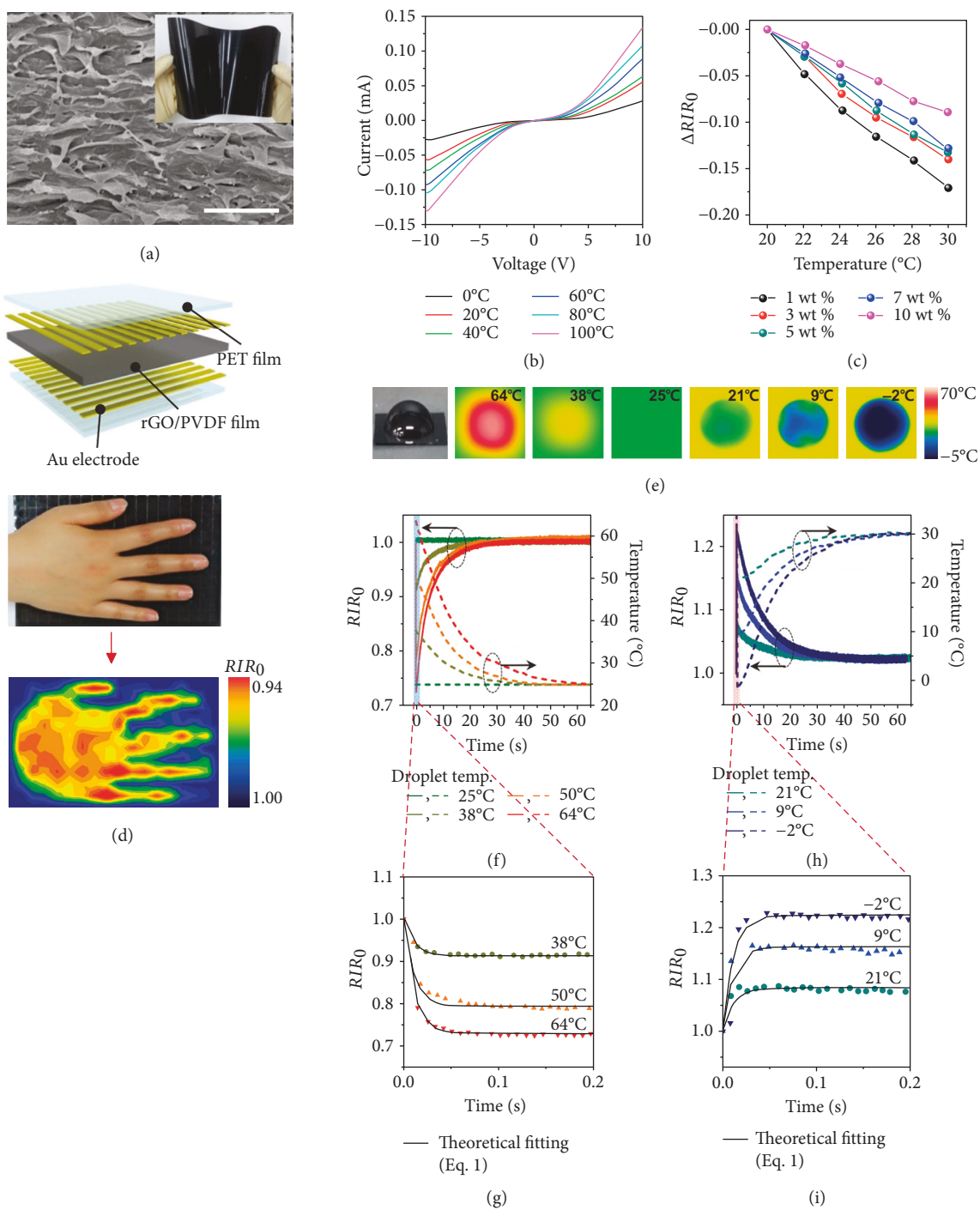


FIGURE 4: (a) Cross-sectional SEM image of the rGO/PVDF composite film with stacked GO sheets (scale bar of $1\ \mu\text{m}$). The inset shows a photograph of a flexible and large-scale ($20 \times 15\ \text{cm}^2$) rGO/PVDF composite film; (b) current-voltage curves of 1 wt % rGO/PVDF composite films at various temperatures; (c) relative resistance change of rGO/PVDF composite film as a function of temperature for various concentrations of rGO; (d) detection of temperature distribution on the human palm: (top) schematic diagram of a sensor array, where the rGO/PVDF composite film is sandwiched between gold electrode arrays (18×12 pixels); (middle) photograph of a human hand on top of the sensor array; (bottom) contour mapping of electrical resistance variations for the local temperature distribution on the human palm; (e) a representative photograph and infrared (IR) camera images of water droplets with different droplet temperatures (64°C to -2°C) on the e-skins; (f and h) relative resistance (R/R_0) and temperature (T) variations of the e-skins after contact with water droplets (f) above room temperature (25°C to 64°C) and (h) below room temperature (-2°C to 21°C); temperature (T) change is measured by an IR camera; (g and i) initial stages of time-domain signals in (f) and (h) showing the variation of relative resistance immediately after contact between e-skins and water droplets; the solid lines represent a fit derived from (4). Reprinted from [70] under the terms of the Creative Commons Attribution-NonCommercial License.

output response of 2.5 μs . The sensor based on PVDF film was used to record a magnitude and spatial distribution of the pressure applied on a human finger during its different modes of movement, i.e., shiatsu, kneading, and rubbing.

The multimodal e-skin containing the rGO/PVDF composite, discussed in the previous section, was applied in [70] for piezoelectric sensing of dynamic tactile stimuli. The interlocked geometry of the e-skin resulted in an increase in generated piezopotential in comparison to conventional piezoelectric films with planar geometry. The evaluated sensitivities of the piezoelectric current of the e-skin on the applied normal forces amounted to 35 $\mu\text{A}/\text{Pa}$ and 5 $\mu\text{A}/\text{Pa}$ for pressures lower and higher than 2.45 kPa, respectively [70]. The e-skin was also employed for detection of sound waveforms from a speaker. It should be underlined that the time-dependent variation of the voltage waveforms of the interlocked e-skins precisely matched the acoustic waveforms from the speaker, corresponding to various letters of the alphabet (“S,” “K,” “I,” and “N”). The amplitude of measured piezoelectric voltage waveforms reached a maximum value at a sound frequency of 2 kHz.

The e-skin based on the rGO/PVDF composite was further arranged in a multilayered flexible ferroelectric sensor of static/dynamic pressure [80]. It exhibited a high performance with ultrahigh pressure sensitivity of 47.7 kPa^{-1} , fast response (20 ms), and a linear sensing characteristic over a wide pressure range (0.0013–353 kPa) [80]. Various types of mechanical stimuli were detected using multilayered rGO/PVDF e-skin, including weak gas flow, acoustic sound, wrist pulse pressure, respiration, and foot pressure.

It was described in [8] that an open-circuit voltage and closed-circuit current were generated in KNbO_3 -PDMS composite due to cyclic bending of this material. Jung et al. [8] provided arguments confirming that these signals actually originated from the piezoelectricity of KNbO_3 . One can see that it is possible to determine the value of dynamic strain applied to the KNbO_3 -PDMS composite up to 0.4% by simply measuring an electrical response of it.

In 2017, Shin et al. [81] fabricated a novel flexible motion sensor using ferroelectric lithium-doped ZnO -PDMS. The sensor was equipped with electrodes made of PEDOT:PSS-functionalized Ag nanowires. This multifunctional device was successfully applied for monitoring of movement and temperature changes. Figure 5 presents a difference between resistive (a) and piezoelectric (b) sensing mechanisms adopted for detection of bending and stretching deformations. Time dependence of generated piezoelectric output voltage and relative electric resistance of the sensor is shown in Figure 5(c). The magnitude of the measured electric signal was 2600% in the case of resistance response to 3 mm long stretching, whereas the bending and stretch motions with speed of 75 mm/s led to generation of open voltages of 1.48 V and 0.47 V, respectively.

In 2016, it was presented for the first time that ferroelectric SbSI nanowires (Figure 6(a)) are suitable for application in shockwave detectors [82]. Before this study, many different bulk ferroelectric materials (e.g., PZT [83, 84] and PZST [85]) have been proposed for use in devices recognizing shock pressure. An electrical response of SbSI nanowires on

impact pressure of 5.9 MPa was investigated (Figure 6(b)). The following exponential function [83] was used for least square fitting of electric field decay after shock compression of SbSI nanowires:

$$E(t) = E(t_0) \exp\left(-\frac{t-t_0}{\tau}\right) \quad \text{for } t > t_0, \quad (5)$$

where $t_0 = 1.14$ ms was the time when the transient of an electric field reached a maximum value and $\tau = 150(5)$ μs represented the recovery time, which was much higher than the response time on pressure impact (<10 μs). It was attributed to long lifetime of depolarizing potential and screening of charges [82]. The stress-induced depolarization of ferroelectric SbSI [82, 86] was responsible for generation of an open-circuit voltage in an investigated material. It should be underlined that the amplitude of an electric field reached the enormous value of $E(t_0) = 2.90(7) \cdot 10^7$ V/m, which was significantly higher than those reported in literature for other ferroelectrics [83–85].

3.3. Piezoresistive Sensing. In order to monitor and distinguish between the temperature and pressure variations, Park et al. developed the ferroelectric e-skin by patterning an interlocked microdome array in the rGO/PVDF composite [70]. They investigated a response of the e-skin resistance to fall of water droplets at different temperatures. It was noticed that an external stress influences deformation, leading to significant change of the contact area between the interlocked microdomes. Due to this strong pressure dependence of contact resistance, the pressure sensitivity of the interlocked microdome arrays was found to be much higher than that of a planar film [70].

4. Photodetectors

Ferroelectric materials that simultaneously possess also semi-conducting properties are recognized as photoferroelectrics [88]. They are sensitive to light illumination, since photons in a semiconductor generate excess free carriers and induce a change in its electronic state. In 2013, Nowak et al. [89] analyzed photoelectrical properties of ferroelectric SbSI xerogel. An investigated sample was composed of a 5 μm thick layer of SbSI nanowires, deposited on the alumina substrate and aligned in the electric field. The Al_2O_3 substrate was equipped with the interdigitated Pt electrodes with spacing of 250 μm . Figure 7(a) presents the spectral dependences of photoconductivity current (I_{PC}) measured for different light intensities. These experimental results were least square fitted with the following semiempirical power equation [88, 89]:

$$I_{\text{PC}}(\lambda, T) = I_{\text{PC0}}(\lambda, T) \cdot I_{\text{L}}^{\gamma(\lambda, T)}, \quad (6)$$

where I_{L} represents the intensity of an incident light and $I_{\text{PC0}}(\lambda, T)$ and $\gamma(\lambda, T)$ denote coefficients dependent on photon energy and temperature. Determined values of the power coefficient γ as a function of light wavelength are shown in Figure 7(b). It was concluded in [88, 89] that obtained results indicated the nonlinear recombination of

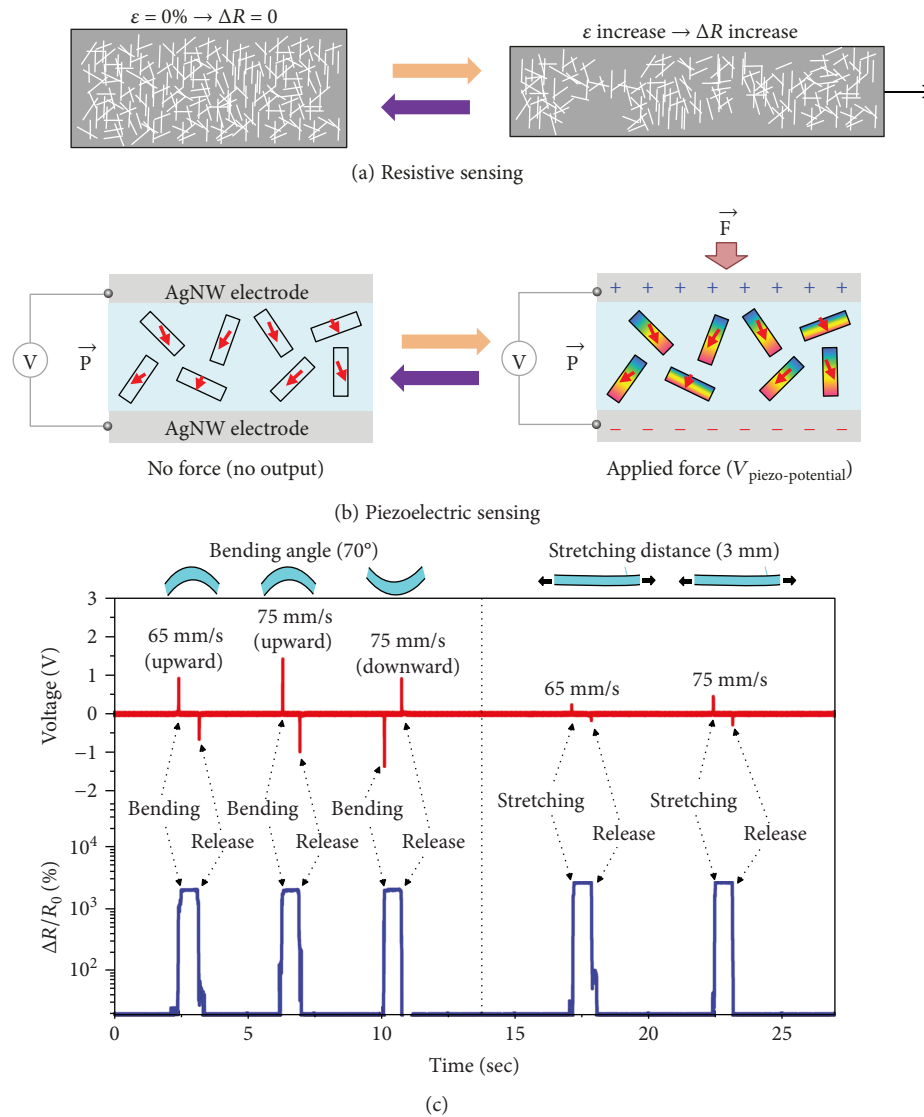


FIGURE 5: Principles of motion detection using a Li-doped ZnO NW-PDMS composite layer. (a) Resistive sensing: the resistance of the AgNW electrode layer changes with the elongation of the AgNW network during bending and stretching motions. (b) Piezoelectric sensing: the piezoelectric output signal is generated between the top and bottom AgNW electrodes when the external force or stress is applied to the device as a result of instantaneous bending and stretching. The piezoelectric output voltage is generated due to polarized Li-doped ZnO NWs packed between the AgNW electrodes. (c) Piezoelectric (top) and resistive (bottom) output measurement for bending (70°) and stretching motions (3 mm) at different speeds. Reprinted with permission from [81]. Copyright (2017) American Chemical Society.

carriers in SbSI nanowires with the increase in excess carrier concentration.

A photoelectric response of an array of a few SbSI nanowires to argon laser illumination ($\lambda = 488$ nm) has been recently investigated (Figure 8(a)). Such device containing a few nanowires of SbSI is presented in Figures 1(c) and 1(d) and described in Section 2.2 of this review. The influence of illumination intensity on photoconductivity current, depicted in Figure 8(b), has been least-squares fitted with (6) in order to determine the values of parameters $\gamma = 0.766$ (61), $I_{PC0} = 1183(52) \cdot 10^{-30}$ A. It should be underlined that the photodetector, based on an array of a few SbSI nanowires, exhibits short response and recovery times (less than 4.5 s).

It should be noted that ferroelectric P(VDF-TrFE) was demonstrated to play a significant role in the development

of photodetectors constructed from a single semiconducting nanowire (e.g., CdS [90] and InP [91]). Its application in polymer side-gated devices resulted in dark current reduction and sensitivity enhancement in comparison to traditional nanowire field-effect transistors. It was due to the fact that intrinsic carriers in a nanowire channel were fully depleted by an ultrahigh electrostatic field arising from polarization of the ferroelectric polymer [90, 91].

Thin films of many different ferroelectric materials ($\text{Pb}_{0.97}\text{La}_{0.03}(\text{Zr}_{0.52}\text{Ti}_{0.48})\text{O}_3$ (PLZT) [92, 93], PZT [94, 95], and $\text{Bi}_4\text{Ti}_3\text{O}_{12}$ [96]) were employed in ultraviolet (UV) sensors. Lai et al. designed and tested a photovoltaic ultraviolet (UV) detector with a unique structure [92]. This device was composed of an in-plane polarized PLZT thin film ($1 \mu\text{m}$) on a transparent silica substrate. The top surface of the

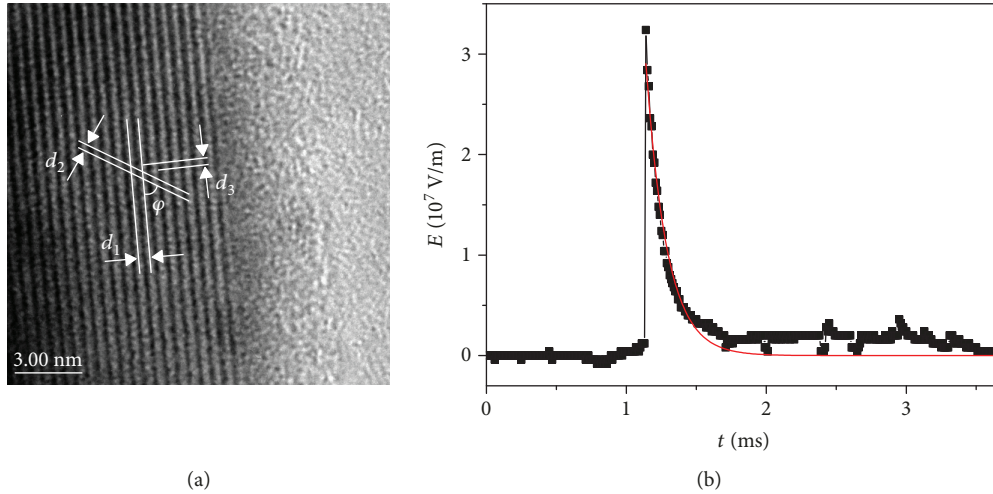


FIGURE 6: (a) A typical HRTEM micrograph of an individual SbSI nanowire from sonochemically prepared xerogel. The fringe spacings of $d_1 = 0.651(5)$ nm, $d_2 = 0.348(5)$, and $d_3 = 0.419(6)$ nm correspond to the interplanar distances of 0.64989, 0.35036, and 0.4160 nm between the (110), (111), and (001) planes of the SbSI crystal [87], respectively. The angle $\varphi = 58.9(4)^\circ$ corresponds to the angle 57.4° between (110) and (111) planes [87]. (b) The transient characteristic of electric field pulse in the SbSI nanodevice induced by shock pressure. Solid red curve represents the fitted relationship (5); values of the fitted parameters are given in the text. Reprinted from [82]. Copyright (2016), with permission from Elsevier.

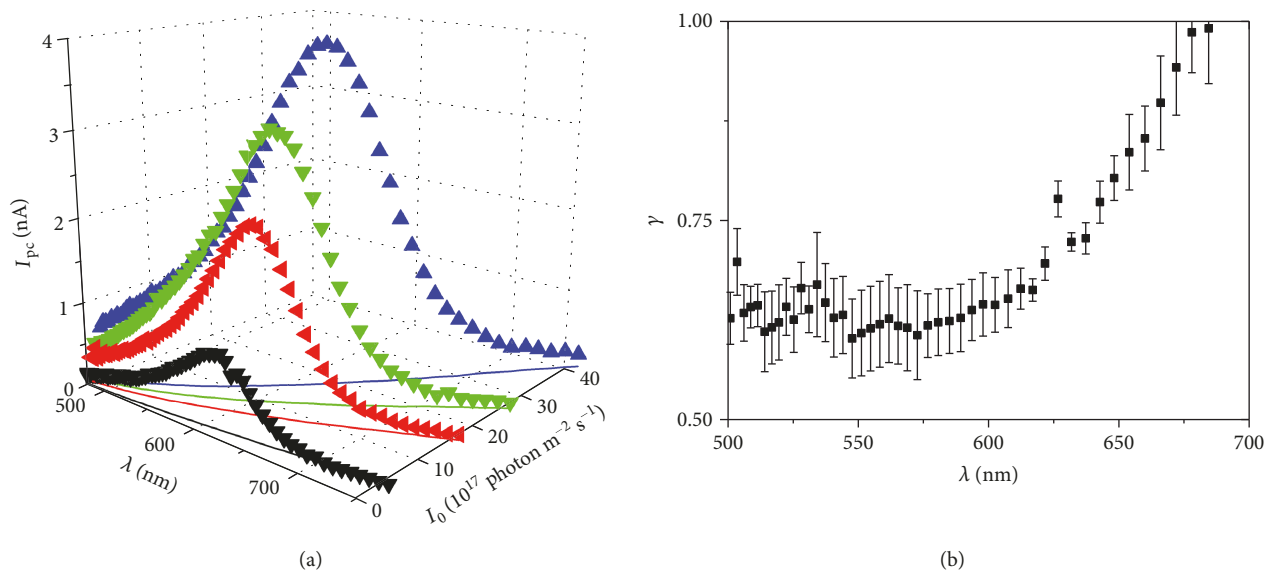


FIGURE 7: (a) Experimental data of spectral dependences of photoconductivity current in SbSI xerogel at 323.7 K ($p = 1.33$ Pa). Solid curves show the spectral dependences of illumination intensities; (b) spectral dependence of (a) power coefficient from (6) least-squares fitted to the experimental data of $I_{PC}(I_0)$ characteristics. Reprinted from [88] under the terms of the Creative Commons Attribution-NonCommercial-ShareAlike 3.0 License.

photodetector was equipped with the interdigital electrodes. A 200 nm thick yttrium-stabilized zirconia (YSZ) was used as a buffer layer between PLZT film and silica substrate. The device was encapsulated in a flip-chip package and hermetically sealed with an epoxy. A response of the back-illuminated photodetector was much higher than the response obtained for irradiation of the PLZT film top surface [92]. The novel device configuration, proposed by Lai et al., enables low-cost, effective, and scratch- and moisture-proof monitoring of UV in harsh conditions.

5. Ionizing Radiation Detectors

One of the new interesting prospective applications of nano-sized ferroelectrics is their use in ionizing radiation detectors. Recently [97], Aguiar et al. have synthesized bismuth sulfoiodide (BiSI) nanostructures via the solvothermal method. BiSI is a ferroelectric semiconductor with the indirect energy band gap of 1.57 eV [98] that belongs to a group of ternary chalcogenide materials. Nanorods of BiSI with dimensions in the range of 100–200 nm were synthesized in monoethylene

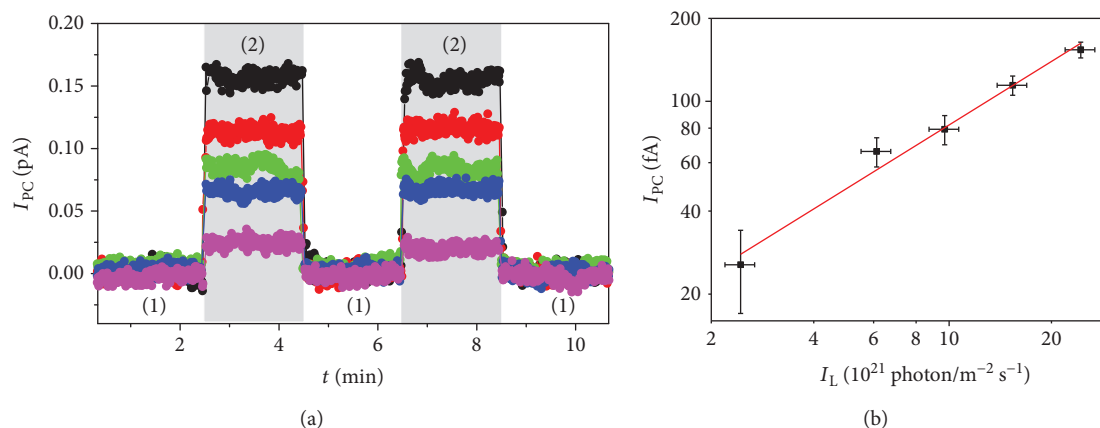


FIGURE 8: (a) Photoconductivity transient characteristics of unilluminated (1) and illuminated (2) array of a few SbSI nanowires for different light intensities: black circle—100% I_{L0} , red circle—63% I_{L0} , green circle—40% I_{L0} , blue circle—25% I_{L0} , pink circle—10% I_{L0} . (b) Influence of illumination intensity on photoconductivity current; red line represents the fitted (6); values of the fitted parameters of (6) are given in the text ($\lambda = 488$ nm, $I_{L0} = 2.4 \cdot 10^{22}$ photon·m⁻² s⁻¹, $E = 2 \cdot 10^6$ V/m, $T = 298$ K, $p = 10^{-2}$ Pa).

glycol in a home-made Teflon-lined autoclave at 453 K during 20 h. The obtained material was compacted into the pellet applying a 15-ton press. Then, gold electrodes were deposited onto the pellet as front and rear electric contacts. Such prepared device was used for detection of X and gamma ray radiation of ²⁴¹Am. The BiSI-based detector exhibited a signal-to-noise relation of 1.4 for an exposure rate of 3.5 mR·h⁻¹ [97]. However, in the case of radiation doses of 0.4 mR·h⁻¹ and 14 mR·h⁻¹, no noticeable response and a behavior corresponding to saturation conditions were observed, respectively.

6. Biosensors

The novel and appealing trend in application of ferroelectric nanomaterials is their use in sensing devices exhibiting a biocompatibility. Nguyen et al. [99] presented that nanoribbons of PbZr_xTi_{1-x}O₃ (PZT) can be exploited to measure mechanical deformations of neuronal cells in response to electrical excitations. In addition, arrays of PZT nanoribbons were transferred onto an elastomer (PDMS) in order to scale to macroscopic areas. Then, they were contacted with interdigitated gold electrodes and poled in the plane of the ribbons. The fabricated device was biointerfaced with the multicellular tissue of an extracted cow lung. Periodic deformations of PZT nanoribbons were evoked by a respiration process, stimulated by a bicycle pump attached to the lung. The magnitudes of voltage and current signals, generated in PZT, exceeded 0.5 V and 3 nA, respectively [99].

Another approach for the application of ferroelectric material in the biosensor was proposed by Li and coworkers [100]. They fabricated a flexural resonant mode diaphragm (FRMD) device. It consisted of a top electrode, a piezoelectric layer (thin film of PZT), a bottom electrode, and a supporting layer. The FRMD sensor was excited by an AC voltage through the converse piezoelectric effect. Oscillatory movement of the diaphragm generated a two-phase ring cycle with a periodic swing. A resonance frequency was determined from an impedance spectrum. Mass loading on

the surface of the sensor led to a shift in resonance frequency. The FRMD sensor based on the thin film of PVDF was able to detect yeast cells in water.

7. Summary and Future Outlook

Low-dimensional ferroelectric materials have been demonstrated as suitable for application in gas sensors for many purposes, including medical diagnosis, early fire detection, indoor air quality monitoring, and control of industrial processes. Sensors based on nanosized ferroelectrics exhibit numerous advantages, including reduced size, small power consumption, reversibility, selectivity, and reliability. It should be underlined that induced or permanent dipole moments of gas molecules interact with the electric polarization of the ferroelectric domains. It supports molecular adsorption on the sensor surface and leads to sensitivity enhancement. Development of the multimodal platforms for gas sensing that can discriminate between different types of gas molecules is a particularly intriguing area for future investigations.

A great potential for application of ferroelectric materials in sensors of different mechanothermal signals has been well documented. The presented cutting-edge devices can detect static and dynamic pressure, strain, temperature changes, surface texture recognition, vibrations, acoustic sound, and shockwaves. In addition, many of the described sensors are able to distinguish between these stimuli via various signal generation modes, i.e., sustained pressure (piezoresistive), temporary pressure (piezoelectric), and temperature changes (pyroelectric). One can predict that development of these smart sensors will result in fast progress in flexible electronics, humanoid robotics, and defense technologies.

One of the interesting prospective directions for future research is fabrication of new ferroelectric nanomaterials and their optimization for use in ionizing radiation detectors. Despite promising values of resistivity, signal-to-noise relation, and sensitivity of BiSI nanorods, they have defects and are not sufficiently homogeneous. Moreover, huge effort

should be made in order to eliminate device saturation and improve the charge transport in the BiSI detector.

The integration of nanosized ferroelectrics into biological systems seems to be especially important for development of medical diagnostic devices and health care monitoring systems. Probably, the ferroelectric self-powered nanosensors will enable measurements of signals arising from such small biological structures as axons or dendrites.

Conflicts of Interest

The author declares that he has no conflicts of interest.

Acknowledgments

This paper was partially supported by Silesian University of Technology (Gliwice, Poland), financial support for young scientists.

References

- [1] J. Valasek, "Piezo-electric and allied phenomena in Rochelle salt," *Physical Review*, vol. 17, no. 4, pp. 475–481, 1920.
- [2] L. Liang, X. Kang, Y. Sang, and H. Liu, "One-dimensional ferroelectric nanostructures: synthesis, properties, and applications," *Advanced Science*, vol. 3, no. 7, article 1500358, 2016.
- [3] J. Varghese, R. W. Whatmore, and J. D. Holmes, "Ferroelectric nanoparticles, wires and tubes: synthesis, characterisation and applications," *Journal of Materials Chemistry C*, vol. 1, no. 15, pp. 2618–2638, 2013.
- [4] S. P. Alpay, V. Nagarajan, and G. A. Rossetti, "Recent developments in ferroelectric nanostructures and multilayers," *Journal of Materials Science*, vol. 44, no. 19, pp. 5021–5024, 2009.
- [5] S. S. Nonnenmann, M. A. Islam, B. R. Beatty, E. M. Gallo, T. McGuckin, and J. E. Spanier, "The ferroelectric field effect within an integrated core/shell nanowire," *Advanced Functional Materials*, vol. 22, no. 23, pp. 4957–4961, 2012.
- [6] X. Liu, Y. Liu, W. Chen, J. Li, and L. Liao, "Ferroelectric memory based on nanostructures," *Nanoscale Research Letters*, vol. 7, no. 1, p. 285, 2012.
- [7] H. Lu, B. Wang, T. Li et al., "Nanodomain engineering in ferroelectric capacitors with graphene electrodes," *Nano Letters*, vol. 16, no. 10, pp. 6460–6466, 2016.
- [8] J. H. Jung, C.-Y. Chen, B. K. Yun et al., "Lead-free KNbO₃ ferroelectric nanorod based flexible nanogenerators and capacitors," *Nanotechnology*, vol. 23, no. 37, article 375401, 2012.
- [9] L. F. Fei, Y. M. Hu, X. Li et al., "Electrospun bismuth ferrite nanofibers for potential applications in ferroelectric photovoltaic devices," *ACS Applied Materials & Interfaces*, vol. 7, no. 6, pp. 3665–3670, 2015.
- [10] M. Qin, K. Yao, and Y. C. Liang, "High efficient photovoltaics in nanoscaled ferroelectric thin films," *Applied Physics Letters*, vol. 93, no. 12, article 122904, 2008.
- [11] A. Renuka Balakrishna and J. E. Huber, "Design optimization of a ferroelectric nano-actuator using phase-field modeling," *MRS Proceedings*, vol. 1674, 2014.
- [12] X. Ren, H. Fan, Y. Zhao, and Z. Liu, "Flexible Lead-free BiFeO₃/PDMS-based nanogenerator as piezoelectric energy harvester," *ACS Applied Materials and Interfaces*, vol. 8, no. 39, pp. 26190–26197, 2016.
- [13] D. Park, S.-H. Shin, I.-J. Yoon, and J. Nah, "Ferroelectric nanoparticle-embedded sponge structure triboelectric generators," *Nanotechnology*, vol. 29, no. 18, article 185402, 2018.
- [14] A. Koka, Z. Zhou, and H. A. Sodano, "Vertically aligned BaTiO₃ nanowire arrays for energy harvesting," *Energy & Environmental Science*, vol. 7, no. 1, pp. 288–296, 2014.
- [15] Y. Yang, J. H. Jung, B. K. Yun et al., "Flexible pyroelectric nanogenerators using a composite structure of lead-free KNbO₃ nanowires," *Advanced Materials*, vol. 24, no. 39, pp. 5357–5362, 2012.
- [16] Y. Xu, C.-H. Cheng, H. Ye, and J. D. Mackenzie, "Electro-optic effect in a nano-crystals doped glass," *Ferroelectrics*, vol. 259, no. 1, pp. 259–268, 2001.
- [17] R. B. Yang, J. Bachmann, E. Pippel et al., "Pulsed vapor-liquid-solid growth of antimony selenide and antimony sulfide nanowires," *Advanced Materials*, vol. 21, no. 31, pp. 3170–3174, 2009.
- [18] J. Varghese, C. O'Regan, N. Deepak, R. W. Whatmore, and J. D. Holmes, "Surface roughness assisted growth of vertically oriented ferroelectric SbSI nanorods," *Chemistry of Materials*, vol. 24, no. 16, pp. 3279–3284, 2012.
- [19] C. Baek, H. Park, J. H. Yun, D. K. Kim, and K.-I. Park, "Lead-free BaTiO₃ nanowire arrays-based piezoelectric energy harvester," *MRS Advances*, vol. 2, no. 56, pp. 3415–3420, 2017.
- [20] Z. Zhou, H. Tang, and H. A. Sodano, "Vertically aligned arrays of BaTiO₃ nanowires," *ACS Applied Materials & Interfaces*, vol. 5, no. 22, pp. 11894–11899, 2013.
- [21] C. C. Bowland, M. H. Malakooti, Z. Zhou, and H. A. Sodano, "Highly aligned arrays of high aspect ratio barium titanate nanowires via hydrothermal synthesis," *Applied Physics Letters*, vol. 106, no. 22, article 222903, 2015.
- [22] K. Page, T. Proffen, M. Niederberger, and R. Seshadri, "Probing local dipoles and ligand structure in BaTiO₃ nanoparticles," *Chemistry of Materials*, vol. 22, no. 15, pp. 4386–4391, 2010.
- [23] S. Li, R. Nechache, C. Harnagea, L. Nikolova, and F. Rosei, "Single-crystalline BiFeO₃ nanowires and their ferroelectric behavior," *Applied Physics Letters*, vol. 101, no. 19, article 192903, 2012.
- [24] G. Z. Wang, S. M. Selbach, Y. D. Yu, X. T. Zhang, T. Grandea, and M. A. Einarsrud, "Hydrothermal synthesis and characterization of KNbO₃ nanorods," *CrystEngComm*, vol. 11, no. 9, pp. 1958–1963, 2009.
- [25] S. Kim, J. H. Lee, J. Lee et al., "Synthesis of monoclinic potassium niobate nanowires that are stable at room temperature," *Journal of American Chemical Society*, vol. 135, no. 1, pp. 6–9, 2013.
- [26] D. Mohanty, G. S. Chaubey, A. Yourdkhani, S. Adireddy, G. Caruntu, and J. B. Wiley, "Synthesis and piezoelectric response of cubic and spherical LiNbO₃ nanocrystals," *RSC Advances*, vol. 2, no. 5, pp. 1913–1916, 2012.
- [27] J. Varghese, S. Barth, L. Keeney, R. W. Whatmore, and J. D. Holmes, "Nanoscale ferroelectric and piezoelectric properties of Sb₂S₃ nanowire arrays," *Nano Letters*, vol. 12, no. 2, pp. 868–872, 2012.
- [28] L. F. Liu, T. Y. Ning, Y. Ren et al., "Synthesis, characterization, photoluminescence and ferroelectric properties of

- PbTiO₃ nanotube arrays,” *Materials Science and Engineering: B*, vol. 149, no. 1, pp. 41–46, 2008.
- [29] C. H. Jeon, Y. S. Lee, K. J. Yee, J. K. Han, and S. D. Bu, “Strain effect on the visible emission in PbTiO₃ nanotubes: template and wall-thickness dependence,” *Current Applied Physics*, vol. 15, no. 2, pp. 115–119, 2015.
- [30] B. D. Stojanovic, C. O. Paiva-Santos, M. Cilense, C. Jovalekic, and Z. Z. Lazarevic, “Structure study of Bi₄Ti₃O₁₂ produced via mechanochemically assisted synthesis,” *Materials Research Bulletin*, vol. 43, no. 7, pp. 1743–1753, 2008.
- [31] A. Baji, Y. W. Mai, Q. Li, and Y. Liu, “Electrospinning induced ferroelectricity in poly(vinylidene fluoride) fibers,” *Nanoscale*, vol. 3, no. 8, pp. 3068–3071, 2011.
- [32] A. Starczewska, M. Nowak, P. Szperlich et al., “Influence of humidity on impedance of SbSI gel,” *Sensors and Actuators A*, vol. 183, pp. 34–42, 2012.
- [33] M. Nowak, A. Nowrot, P. Szperlich et al., “Fabrication and characterization of SbSI gel for humidity sensors,” *Sensors and Actuators A*, vol. 210, pp. 119–130, 2014.
- [34] M. Nowak, K. Mistewicz, A. Nowrot, P. Szperlich, M. Jesionek, and A. Starczewska, “Transient characteristics and negative photoconductivity of SbSI humidity sensor,” *Sensors and Actuators A: Physical*, vol. 210, pp. 32–40, 2014.
- [35] K. Mistewicz, M. Nowak, R. Paszkiewicz, and A. Guiseppi-Elie, “SbSI nanosensors: from gel to single nanowire devices,” *Nanoscale Research Letters*, vol. 12, no. 1, pp. 97–104, 2017.
- [36] M. J. Polking, A. P. Alivisatos, and R. Ramesh, “Synthesis, physics, and applications of ferroelectric nanomaterials,” *MRS Communications*, vol. 6, no. 1, pp. f1–f4, 2015.
- [37] L. W. Martin and A. M. Rappe, “Thin-film ferroelectric materials and their applications,” *Nature Reviews Materials*, vol. 2, no. 2, article 16087, 2016.
- [38] X. Chen, X. Han, and Q.-D. Shen, “PVDF-based ferroelectric polymers in modern flexible electronics,” *Advanced Electronic Materials*, vol. 3, no. 5, article 1600460, 2017.
- [39] G. Schwartz, B. C.-K. Tee, J. Mei et al., “Flexible polymer transistors with high pressure sensitivity for application in electronic skin and health monitoring,” *Nature Communications*, vol. 4, no. 1, 1859.
- [40] S. J. Benight, C. Wang, J. B. H. Tok, and Z. Bao, “Stretchable and self-healing polymers and devices for electronic skin,” *Progress in Polymer Science*, vol. 38, no. 12, pp. 1961–1977, 2013.
- [41] I. Bretos, R. Jiménez, A. Wu, A. I. Kingon, P. M. Vilarinho, and M. L. Calzada, “Activated solutions enabling low-temperature processing of functional ferroelectric oxides for flexible electronics,” *Advanced Materials*, vol. 26, no. 9, pp. 1405–1409, 2014.
- [42] N. Martín-Arbella, I. Bretos, R. Jiménez, M. L. Calzada, and R. Sirera, “Metal complexes with N-methyldiethanolamine as new photosensitive precursors for the low-temperature preparation of ferroelectric thin films,” *Journal of Materials Chemistry*, vol. 21, no. 25, pp. 9051–9059, 2011.
- [43] I. Bretos, R. Jiménez, D. Pérez-Mezcua, N. Salazar, J. Ricote, and M. L. Calzada, “Low-temperature liquid precursors of crystalline metal oxides assisted by heterogeneous photocatalysis,” *Advanced Materials*, vol. 27, no. 16, pp. 2608–2613, 2015.
- [44] M. Tomczyk, I. Bretos, R. Jiménez et al., “Direct fabrication of BiFeO₃ thin films on polyimide substrates for flexible electronics,” *Journal of Materials Chemistry C*, vol. 5, no. 47, pp. 12529–12537, 2017.
- [45] J. M. Gregg, “Ferroelectrics at the nanoscale,” *Physica Status Solidi A*, vol. 206, no. 4, pp. 577–587, 2009.
- [46] D. Li, M. H. Zhao, J. Garra et al., “Direct in situ determination of the polarization dependence of physisorption on ferroelectric surfaces,” *Nature Materials*, vol. 7, no. 6, pp. 473–477, 2008.
- [47] L. Y. Kraya and R. Kraya, “Polarization dependence of molecular adsorption on ferroelectrics,” *Acta Crystallographica Section B*, vol. B69, pp. 105–109, 2013.
- [48] V. M. Fridkin and S. Ducharme, “Ferroelectricity at the nanoscale,” *Physics-Uspekhi*, vol. 57, no. 6, pp. 597–603, 2014.
- [49] L. Wang, K. Kalyanasundaram, M. Stanacevic, and P. Gouma, “Nanosensor device for breath acetone detection,” *Sensor Letters*, vol. 8, no. 5, pp. 709–712, 2010.
- [50] O. Copie, N. Chevalier, G. Le Rhun et al., “Adsorbate screening of surface charge of microscopic ferroelectric domains in sol-gel PbZr_{0.2}Ti_{0.8}O₃ thin films,” *ACS Applied Materials and Interfaces*, vol. 9, no. 34, pp. 29311–29317, 2017.
- [51] M. A. Khan, M. A. Nadeem, and H. Idriss, “Ferroelectric polarization effect on surface chemistry and photo-catalytic activity: a review,” *Surface Science Reports*, vol. 71, no. 1, pp. 1–31, 2016.
- [52] J. Garra, J. M. Vohs, and D. A. Bonnell, “The effect of ferroelectric polarization on the interaction of water and methanol with the surface of LiNbO₃ (0001),” *Surface Science*, vol. 603, no. 8, pp. 1106–1114, 2009.
- [53] A. Kakekhani, S. Ismail-Beigi, and E. I. Altman, “Ferroelectrics: a pathway to switchable surface chemistry and catalysis,” *Surface Science*, vol. 650, pp. 302–316, 2016.
- [54] Y. Yun, L. Kampschulte, M. Li, D. Liao, and E. I. Altman, “Effect of ferroelectric poling on the adsorption of 2-propanol on LiNbO₃ (0001),” *Journal of Physical Chemistry C*, vol. 111, no. 37, pp. 13951–13956, 2007.
- [55] V. B. Kapustianik, S. A. Sveleba, R. Tchukvinskiy et al., “Dielectric properties and electric conductivity of dimethylammonium tetrachlorocobaltate ferroelectric crystals,” *Physica Status Solidi A*, vol. 151, no. 2, pp. 481–488, 1995.
- [56] K. Mistewicz, M. Nowak, R. Wrzalik, J. Ślezionek, J. Wiczorek, and A. Guiseppi-Elie, “Ultrasonic processing of SbSI nanowires for their application to gas sensors,” *Ultrasonics*, vol. 69, pp. 67–73, 2016.
- [57] K. Mistewicz, M. Nowak, P. Szperlich, M. Jesionek, and R. Paszkiewicz, “SbSI single nanowires as humidity sensors,” *Acta Physica Polonica A*, vol. 126, no. 5, pp. 1113–1114, 2014.
- [58] K. Mistewicz, M. Nowak, A. Starczewska et al., “Determination of electrical conductivity type of SbSI nanowires,” *Materials Letters*, vol. 182, pp. 78–80, 2016.
- [59] R. Ganeshkumar, K. V. Sopiha, P. Wu, C. Wei Cheah, and R. Zhao, “Ferroelectric KNbO₃ nanofibers: synthesis, characterization and their application as a humidity nanosensor,” *Nanotechnology*, vol. 27, no. 39, article 395607, 2016.
- [60] Y. V. Popik, V. N. Zhikharev, and V. V. Betsa, “Effect of adsorption on the polarization processes in the ferroelectric semiconductors BaTiO₃ and SbSI,” *Fizika Tverdogo Tela*, vol. 24, pp. 486–493, 1982.
- [61] O. K. Tan, W. Zhu, M. S. Tse, and X. Yao, “Hydrogen-sensitive I–V characteristics of metal-ferroelectric gas sensor device fabricated by sol-gel technique,” *Materials Science and Engineering B*, vol. 58, no. 3, pp. 221–228, 1999.

- [62] X. F. Chen, W. G. Zhu, and O. K. Tan, "Microstructure, dielectric properties and hydrogen gas sensitivity of sputtered amorphous $\text{Ba}_{0.67}\text{Sr}_{0.33}\text{TiO}_3$ thin films," *Materials Science and Engineering B*, vol. 77, no. 2, pp. 177–184, 2000.
- [63] O. K. Tan, X. F. Chen, and W. Zhu, "Amorphous ferroelectric thin film capacitive device for hydrogen detection," *Journal of Materials Science*, vol. 38, no. 21, pp. 4353–4363, 2003.
- [64] J. Deng, W. Zhu, O. K. Tan, and X. Yao, "Amorphous $\text{Pb}(\text{Zr}, \text{Ti})\text{O}_3$ thin film hydrogen gas sensor," *Sensors and Actuators B*, vol. 77, no. 1–2, pp. 416–420, 2001.
- [65] K. Mistewicz, M. Nowak, D. Stróż, and A. Guiseppi-Elie, "Ferroelectric SbSI nanowires for ammonia detection at a low temperature," *Talanta*, vol. 189, pp. 225–232, 2018.
- [66] S.-K. Lee, D. Chang, and S. W. Kim, "Gas sensors based on carbon nanoflake/tin oxide composites for ammonia detection," *Journal of Hazardous Materials*, vol. 268, pp. 110–114, 2014.
- [67] B. Chakradhar Sridhar, M. Sasikala, J. Husain, M. V. N. Pradeep, and M. V. N. Ambika Prasad, "Synthesis, characterization, electrical and sensor behavior of PANI/ In_2O_3 nano composites," *Ferroelectrics*, vol. 502, no. 1, pp. 159–169, 2016.
- [68] A. N. Morozovska, E. A. Eliseev, G. S. Svechnikov, and S. V. Kalinin, "Pyroelectric response of ferroelectric nanowires: size effect and electric energy harvesting," *Journal of Applied Physics*, vol. 108, no. 4, article 042009, 2010.
- [69] M. Zirkl, A. Sawatdee, U. Helbig et al., "An all-printed ferroelectric active matrix sensor network based on only five functional materials forming a touchless control interface," *Advanced Materials*, vol. 23, no. 18, pp. 2069–2074, 2011.
- [70] J. Park, M. Kim, Y. Lee, H. Sang Lee, and H. Ko, "Fingertip skin-inspired microstructured ferroelectric skins discriminate static/dynamic pressure and temperature stimuli," *Science Advances*, vol. 1, no. 9, pp. e1500661–e1500613, 2015.
- [71] P. Murali, "Ferroelectric thin films for micro-sensors and actuators: a review," *Journal of Micromechanics and Microengineering*, vol. 10, no. 2, pp. 136–146, 2000.
- [72] P. Murali, R. G. Polcawich, and S. Trolrier-McKinstry, "Piezoelectric thin films for sensors, actuators, and energy harvesting," *MRS Bulletin*, vol. 34, no. 9, pp. 658–664, 2009.
- [73] I. Kanno, "Piezoelectric MEMS: ferroelectric thin films for MEMS applications," *Japanese Journal of Applied Physics*, vol. 57, no. 4, article 040101, 2018.
- [74] N. Ledermann, P. Murali, J. Baborowski et al., " $\{1\ 0\ 0\}$ -textured, piezoelectric $\text{Pb}(\text{Zr}_x, \text{Ti}_{1-x})\text{O}_3$ thin films for MEMS: integration, deposition and properties," *Sensors and Actuators A*, vol. 105, no. 2, pp. 162–170, 2003.
- [75] T. Zhang, H. Li, C. Zhou et al., "Ferroelectricity, piezoelectricity, and dielectricity of 0.06PMnN-0.94PZT(45/55) thin film on silicon substrate," *Journal of Nanomaterials*, vol. 2015, Article ID 864591, 6 pages, 2015.
- [76] Y. Qiu, J. V. Gigliotti, M. Wallace et al., "Piezoelectric micromachined ultrasound transducer (PMUT) arrays for integrated sensing, actuation and imaging," *Sensors*, vol. 15, no. 4, pp. 8020–8041, 2015.
- [77] I. Graz, M. Kaltenbrunner, C. Keplinger et al., "Flexible ferroelectret field-effect transistor for large-area sensor skins and microphones," *Applied Physics Letters*, vol. 89, no. 7, article 073501, 2006.
- [78] S. Bauer, R. Gerhard-Mulhaupt, and G. M. Sessler, "Ferroelectrets: soft electroactive foams for transducers," *Physics Today*, vol. 57, no. 2, pp. 37–43, 2004.
- [79] K. Lu, W. Huang, J. Guo et al., "Ultra-sensitive strain sensor based on flexible poly(vinylidene fluoride) piezoelectric film," *Nanoscale Research Letters*, vol. 13, no. 1, pp. 83–88, 2018.
- [80] Y. Lee, J. Park, S. Cho et al., "Flexible ferroelectric sensors with ultrahigh pressure sensitivity and linear response over exceptionally broad pressure range," *ACS Nano*, vol. 12, no. 4, pp. 4045–4054, 2018.
- [81] S.-H. Shin, D. Hoon Park, J.-Y. Jung, M. H. Lee, and J. Na, "Ferroelectric zinc oxide nanowire embedded flexible sensor for motion and temperature sensing," *ACS Applied Materials & Interfaces*, vol. 9, no. 11, pp. 9233–9238, 2017.
- [82] K. Mistewicz, M. Nowak, D. Stróż, and R. Paszkiewicz, "SbSI nanowires for ferroelectric generators operating under shock pressure," *Materials Letters*, vol. 180, pp. 15–18, 2016.
- [83] S. T. Montgomery, R. M. Brannon, J. Robbins, R. E. Setchell, and D. H. Zeuch, "Simulation of the effects of shock stress and electrical field strength on shock-induced depoling of normally poled PZT 95/5," *AIP Conference Proceedings*, vol. 620, pp. 201–204, 2002.
- [84] P. C. Lysne and C. M. Percival, "Electric energy generation by shock compression of ferroelectric ceramics: Normal-mode response of PZT 95/5," *Journal of Applied Physics*, vol. 46, no. 4, pp. 1519–1525, 1975.
- [85] D. Jiang, Y. Feng, J. Du, and Y. Gu, "Effects of shock pressure and self-generated electric field on shock-induced ferroelectric to antiferroelectric phase transition in lead zirconate stannate titanate ferroelectric ceramics," *Journal of Advanced Dielectrics*, vol. 2, no. 4, article 1250026, 2012.
- [86] L. L. Altgilbers, J. Baird, B. L. Freeman, C. S. Lynch, and S. I. Shkuratov, *Explosive Pulsed Power*, Imperial College Press, London, 2011.
- [87] *Antimony Sulfide Iodide, JCPDS-International Centre for Diffraction Data, PCPDFWIN v.2.1, card file no.74-0149*, 2000.
- [88] M. Nowak, "Photoferroelectric nanowires," in *Nanowires Science and Technology*, N. Lupu, Ed., pp. 269–308, Intech, Croatia, 2010.
- [89] M. Nowak, Ł. Bober, B. Borkowski et al., "Quantum efficiency coefficient for photogeneration of carriers in SbSI nanowires," *Optical Materials*, vol. 35, no. 12, pp. 2208–2216, 2013.
- [90] D. Zheng, H. Fang, P. Wang et al., "High-performance ferroelectric polymer side-gated CdS nanowire ultraviolet photodetectors," *Advanced Functional Materials*, vol. 26, no. 42, pp. 7690–7696, 2016.
- [91] D. Zheng, J. Wang, W. Hu et al., "When nanowires meet ultrahigh ferroelectric field – high-performance full-depleted nanowire photodetectors," *Nano Letters*, vol. 16, no. 4, pp. 2548–2555, 2016.
- [92] S. C. Lai, K. Yao, Y. F. Chen, L. Zhang, and Y.-F. Lim, "A photovoltaic UV sensor with a ferroelectric thin film on transparent substrate," *IEEE Electron Device Letters*, vol. 34, no. 11, pp. 1427–1429, 2013.
- [93] B. K. Gan, K. Yao, S. C. Lai, Y. F. Chen, and P. C. Goh, "An ultraviolet (UV) detector using a ferroelectric thin film with in-plane polarization," *IEEE Electron Device Letters*, vol. 29, no. 11, pp. 1215–1217, 2008.

- [94] G. Suchanek and G. Gerlach, "Ferroelectric–semiconductor UV sensors," *Physica Status Solidi A*, vol. 185, no. 1, pp. 115–120, 2001.
- [95] R. Gupta, M. Tomar, and V. Gupta, "Optical tuning of electrical properties of PZT thin film deposited on STO," in *International Workshop on Thin Films for Electronics, Electro-Optics, Energy, and Sensors*, vol. 966703, Suzhou, China, November 2015.
- [96] L. Pintilie, M. Alexe, A. Pignolet, and D. Hesse, "Bi₄Ti₃O₁₂ ferroelectric thin film ultraviolet detectors," *Applied Physics Letters*, vol. 73, no. 3, pp. 342–344, 1998.
- [97] I. Aguiar, M. Mombrú, M. Pérez Barthaburu, H. Bentos Pereira, and L. Fornaro, "Influence of solvothermal synthesis conditions in BiSI nanostructures for application in ionizing radiation detectors," *Materials Research Express*, vol. 3, no. 2, article 025012, 2016.
- [98] A. Audzijonis, R. Žaltauskas, R. Sereika, L. Žigas, and A. Rēza, "Electronic structure and optical properties of BiSI crystal," *Journal of Physics and Chemistry of Solids*, vol. 71, no. 6, pp. 884–891, 2010.
- [99] T. D. Nguyen, N. Deshmukh, J. M. Nagarah et al., "Piezoelectric nanoribbons for monitoring cellular deformations," *Nature Nanotechnology*, vol. 7, no. 9, pp. 587–593, 2012.
- [100] S. Li, W. Ren, X. Lu et al., "Ferroelectric thin film diaphragm resonators for bio-detection," *Ferroelectrics*, vol. 410, no. 1, pp. 145–151, 2010.



Hindawi
Submit your manuscripts at
www.hindawi.com

